J Mater Sci (2023) 58:10516–10538

Metals & corrosion

Thermodynamic description of the Al–Ag–Zr system and discovery of the high-strength ternary phase $Al_{1.84}Ag_{0.16}Zr$

Zixuan Deng[1], Yanjun Ding[1], Patrick J. Masset[2], Kaige Wang[1], Ligang Zhang[1,*], and Libin Liu[1,*]

[1] *School of Material Science and Engineering, Central South University, Changsha 410083, Hunan, People's Republic of China*
[2] *Faculty of Materials Science and Engineering, Warsaw University of Technology, Woloska 141, 02-507 Warsaw, Poland*

Received: 30 March 2023
Accepted: 2 June 2023

ABSTRACT

The investigation of the Al–Ag–Zr system is crucial for the development of heat-resistant Al alloys, which are essential for applications in high-temperature environments. In this work, we first determined the isothermal sections of the Al–Ag–Zr system at 500 and 600 °C using equilibrium alloys. Simultaneously, the τ_3 (Al_6AgZr_6) phase was identified by transmission electron microscopy (TEM). In addition, the three-phase equilibrium of τ_3 + AgZr + (Ag) instead of Al_3Zr_4 + AgZr + (Ag) was confirmed at 500 and 600 °C. The formation enthalpies of the end-members and ternary compounds in the Al–Ag–Zr system were calculated via first-principles calculations. Based on the experimental and computational results, a thermodynamic database of the Al–Ag–Zr system was established using the CALPHAD (calculation of phase diagrams) method. The hardness of τ_1 ($Al_{2.68}Ag_{0.32}Zr$) and τ_2 ($Al_{1.84}Ag_{0.16}Zr$) were determined to be 3.82 and 10.20 GPa, respectively, using nanoindentation. The introduction of the τ_2 phase in the design of Al alloys can considerably increase the mechanical properties of the alloys.

Introduction

Aluminum alloys are commonly strengthened using methods such as solid solution strengthening [1, 2], grain refinement strengthening [3], work hardening [4, 5], second phase strengthening [6, 7], and heterostructure strengthening [8–10]. In practical applications, multiple strengthening methods are often combined to optimize alloy performance. Adding alloying elements to aluminum alloys can form heterostructures or introduce second phases to improve their heat resistance and strength. For example, in Al–Sc–Zr alloys, core–shell nanoparticles with a Sc-rich core and a Zr-rich shell about 1–2 nm

---

Handling Editor: P. Nash.

Address correspondence to E-mail: ligangzhang@csu.edu.cn; lbliu@csu.edu.cn

Springer

https://doi.org/10.1007/s10853-023-08665-3

thickness can precipitate. These nanoparticles can provide the alloys with high strength and excellent thermal stability [11]. The addition of equal amounts of Fe and Ni to Al–Cu–Mg alloys introduces a stable dispersed strengthening Al_9FeNi phase [6]. This phase exhibits hardness values of 7.71 GPa and 5.83 GPa at room temperature and 350 °C, respectively, which are higher than that of Al_2Cu at room temperature (5.77 GPa) [12]. Therefore, the introduction of Al_9FeNi can considerably improve the mechanical properties of the alloy. Currently, the most used Al–Cu–Mg–Fe–Ni alloy is 2618, which retains good mechanical properties above 200 °C. Adding Mn to Al–Cu alloys can form a dispersed $Al_{20}Cu_2Mn_3$ phase [13]. The high-temperature creep resistance of an Al–Cu–Mn alloy reinforced by coarse $Al_{20}Cu_2Mn_3$ phases is better than that of Al–Cu–Mg alloys consisting of small θ' phases [7].

Using phase diagrams to guide the design of heat-resistant aluminum alloys can reduce time and cost [14]. Zirconium, a transition element, is one of the microalloying elements commonly used in Al–Cu–Mg–Ag alloys [15, 16]. Kotur et al. [17] experimentally verified the existence of τ_1 and τ_2 ternary phases in the Al–Ag–Zr system. Currently, reports on the thermodynamic data and phase properties of the ternary phases in the Al–Ag–Zr system are limited [17, 18]. Understanding the phase equilibrium and thermodynamic properties of the Al–Ag–Zr system is crucial for designing alloy compositions and developing heat treatment regimes. In this work, the isothermal sections of the Al–Ag–Zr system at 500 and 600 °C were determined experimentally. The enthalpy of formation of phases such as τ_1 and τ_2 was calculated via first-principles calculations, and a thermodynamic database for the Al-Ag–Zr system was established. Additionally, the hardness of the τ_1 and τ_2 ternary phases was measured to provide theoretical references for studying the effect of the introduction of the second phases on the properties of aluminum alloys.

Literature review

The Al–Ag system

An evaluation of the Al–Ag system can be found in our recent report [14], and the thermodynamic parameters reported by Wit et al. [19] were used in this work. The corresponding Al–Ag binary phase diagram is shown in Fig. 1.

The Al–Zr system

The Al–Zr binary phase diagram [20] is shown in Fig. 1. In this system, 10 stable intermetallic compounds are listed: $AlZr_3$, $AlZr_2$, Al_3Zr_5, Al_2Zr_3, Al_3Zr_4, Al_4Zr_5, AlZr, Al_3Zr_2, Al_2Zr and Al_3Zr. In 1954, McPherson et al. [21] conducted the first systematic investigation of the Al–Zr phase diagram using metallographic methods, X-ray diffraction (XRD) and thermal analysis. Later, Peruzzi [22] re-determined the phase diagram of the Zr-rich region at 500–1300 °C via metallography, XRD, electron probe analysis, and resistance measurement. The samples used by Peruzzi are of higher purity than those used in previous experiments, and the phase diagrams are very reliable. Saunders [23, 24] evaluated the Al–Zr system twice, but neither evaluation considered the Al_3Zr_4 phase. In 2001, Wang et al. [25] used a new thermodynamic model to evaluate the Al–Zr binary system, and the calculated enthalpy of formation of the compound was in good agreement with the experimental data. However, Wang et al. [25] did not apply any thermodynamic constraint to the Zr-rich intermetallic compounds. Therefore, Fischer and Colinet [20] reassessed the Al–Zr binary system, attributing high reliability to the ab-initio results.

The Ag–Zr system

Figure 1 also shows the binary phase diagram of the Ag–Zr system [26]. Two intermetallic compounds AgZr and $AgZr_2$ exist. Raub et al. [27] measured the liquidus and solid solubility curve in the 4–51 at.% Zr phase region and found that the eutectic reaction L Ag + AgZr occurred at 955 °C. Betterton et al. [28] studied the phase diagram of the Zr-rich region and proved the existence of intermetallic compounds AgZr and $AgZr_2$, and measured the eutectoid reaction (βZr) ↔ (αZr) + $AgZr_2$. Zhang [29] et al. surveyed the phase diagram of the Zr content in the 20–80 at.% range via thermal analysis. Karakaya et al. [30] optimized the Ag–Zr system but ignored the experimental data of Zhang et al. [29] in the optimization process. In 2010, Kang et al. [31] evaluated Ag–Zr system using a modified quasi-chemical solution model of FactSage [32], but this model only works with FactSage and is not compatible with

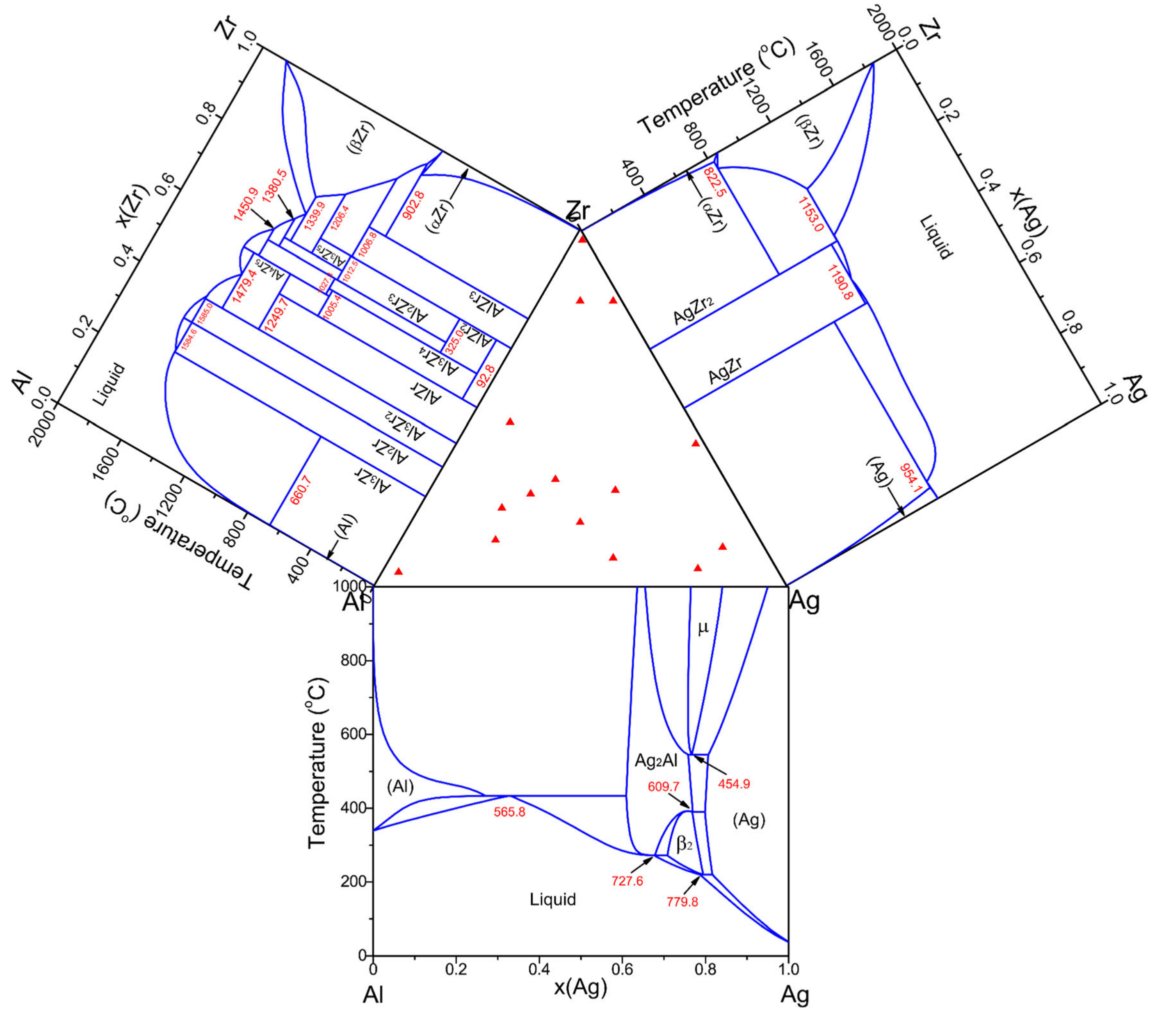

Figure 1 Binary Al–Ag [19], Al–Zr [20], and Ag–Zr [26] phase diagrams calculated with the thermodynamic datasets from the literature. The red triangles mark the alloy composition designed to determine the isothermal section.

Pandat [33] and Thermo-Calc [34]. In 2016, Hsiao et al. [26] re-evaluated the Ag–Zr system, and most of the calculated data are consistent with the experimental data.

The Al–Ag–Zr ternary system

The isothermal section of the Al–Ag–Zr ternary system at 500 °C was first described by Kotur et al. [17] in 2003. Three ternary intermetallic compounds exist in this system: τ_1 ($AuCu_3$ structure type), τ_2 ($MgCu_2$), and τ_3 (W_6Fe_7). Recently, Hsiao et al. [18] also determined the isothermal section of Al–Ag–Zr ternary system at 500 °C using the equilibrium alloy method, and confirmed the existence of τ_2 and τ_3. A comparison of the experimental results of Kotur et al. and Hsiao et al. indicates that Hsiao et al. suggest that $AgZr_2$ and AgZr are stoichiometric compounds, whereas Kotur et al. suggest that they comprise a certain range of solid solution. In addition, Hsiao et al. measured the phase equilibria at the Zr-rich region as $AlZr_2 + AgZr_2 + AgZr$, $AlZr_2 + AgZr + Al_2Zr_3$, and $Al_2Zr_3 + AgZr + Al_3Zr_4$, which differs from the results of Kotur et al. Earlier, Rieger [35] had reported that $AlAg_2Zr_3$ existed stably at 850 °C or 1100 °C, but the existence of an $AlAg_2Zr_3$ phase was not detected in the experiments by Kotur et al. and Hsiao et al. Because few studies exist on the Al–Ag–Zr ternary system, the thermodynamic data of the intermediate compounds are also very limited. Therefore, in this work, the isothermal sections of the Al–Ag–Zr system at 500 and 600 °C were further investigated using equilibrium alloys annealed for a longer time. The data on the crystallographic structure of each phase in the Al–Ag–Zr system are given in Table 1.

Experimental procedure

Alloy samples preparations

The isothermal sections of Al–Ag–Zr at 500 and 600 °C were extrapolated via the Thermo-Calc software [34] using databases [19, 20, 26] without any ternary parameters.

Using Al, Ag, and Zr of 99.99 wt% purity from Beijing Jinyu as the raw materials, fifteen individual 10 g alloys samples, were prepared via arc melting under argon protection. Table 2 lists their nominal compositions, which were chosen to place them in different phase regions. During alloy preparation, a titanium ball was used as an oxygen getter, and all alloys were turned six times after each melting round to ensure homogeneity. The as-melted samples were divided into two pieces, sealed in argon-filled quartz tubes, and placed in a diffusion furnace (KSL-1700X, Shenyang Kejin) at 500 °C for 120 days and 600 °C for 90 days, respectively.

Composition and phase equilibrium analysis

After annealing, the alloy samples were quenched in cold water and observed using a scanning electron microscope (SEM, FEI Quanta FEG 250) equipped with an energy dispersive X-ray spectrometer (EDS, AZtec X-Max 80) to investigate the alloy morphology. Electron probe microanalyzer (EPMA, JXA-8100 F) was performed at 20 kV and 20 nA using the pure elements as standards. X-ray diffraction (XRD, (Advance D8) was conducted on ground alloy powders under Cu-Kα radiation at 40 kV and 40 mA with a scan rate of 5°/min. The alloys were characterized

Table 1 Crystal structure data on the equilibrium phases in the Al–Ag–Zr system

Phase	Pearson symbol	Space group	Proto-type	Lattice parameter (Å)			Comments/ T (°C)	References
				a	b	c		
(Al)	*cF*4	$Fm\bar{3}m$	Cu	4.049	–	–	Pure Al	[36]
(Ag)	cF4	$Fm\bar{3}m$	Cu	4.085	–	–	Pure Ag	[36]
ζ (Ag_2Al)	*hP*2	$P6_3/mmc$	Mg	2.878	–	4.622	27–43 at.% Al < 727	[36]
μ (Ag_3Al-r)	*cP*20	P_4132	Mn	6.942	–	–	21–26 at.% Al < 448	[37]
$β_2$ (Ag_3Al-h)	*cI*2	$Im\bar{3}m$	W	3.240	–	–	21–30 at.% Al 610–780	[37]
(αZr)	*hP*2	$P6_3/mmc$	Mg	3.232	–	5.148	Pure Zr < 863	[38]
(βZr)	*cI*2	$Im\bar{3}m$	W	3.609	–	–	Pure Zr 863–1855	[39]
Al_3Zr	*tI*16	$I4/mmm$	Al_3Zr	4.010	–	17.300	< 1580	[40]
Al_2Zr	*hP*12	$P6_3/mmc$	$MgZn_2$	5.280	–	8.748	< 1660	[40]
Al_3Zr_2	*oF*40	$Fdd2$	Al_3Zr_2	9.601	13.910	5.578	< 1590	[40]
AlZr	*oC*8	$Cmcm$	CrB	3.360	10.890	4.270	< 1275	[40]
Al_4Zr_5	*hP*18	$P6_3/mcm$	Ga_4Ti_5	8.447	–	5.785	1000–1550	[40]
Al_3Zr_4	*hP*7	$P6/mmm$	Al_3Zr_4	5.430	–	5.390	< 1030	[40]
Al_2Zr_3	*tP*20	$P4_2/mnm$	Al_2Zr_3	7.632	–	6.997	< 1480	[40]
Al_3Zr_5	*tI*32	$I4/mcm$	Si_3W_5	11.042	–	5.393	1012–1380	[40]
$AlZr_2$	*hP*6	$P6_3/mmc$	$InNi_2$	4.882	–	5.918	< 1350	[40]
$AlZr_3$	*cP*4	$Pm\bar{3}m$	$AuCu_3$	4.373	–	–	< 1019	[41]
AgZr	*tP*4	$P4/nmc$	γ-CuNi	3.471		6.603	< 1135	[29]
$AgZr_2$	*tI*6	$I4/mmm$	$MoSi_2$	3.265		12.030	< 1190	[42]
$τ_1$ ($Al_{2.68}Ag_{0.32}Zr$)	*cP*4	$Pm\bar{3}m$	Al_3Cu	4.102	–	–		[17]
$τ_2$ ($Al_{1.84–1.69}Ag_{0.16–0.31}Zr$)	cF24	$Fd\bar{3}m$	$MgCu_2$	7.515	–	–		[17]
$τ_3$ ($Al_{5.70–5.18}Ag_{1.30–1.82}Zr$)	*hR*39	$R\bar{3}m$	W_6Fe_7	5.393	–	29.093		[17]

Table 2 Equilibrium phase constitution and compositions of constituent phases measured in the annealed Al–Ag–Zr alloys at 500 °C

Alloy No.	Nominal composition (at.)			EPMA analyzed composition (at.)			Phase determination
	Al	Ag	Zr	Al	Ag	Zr	
1#	0.01	0.02	0.97	0.01	0.02	0.97	(αZr)
2#	0.02	0.18	0.8	0.02	0.04	0.94	(αZr)
				0.01	0.32	0.67	$AgZr_2$
3#	0.02	0.58	0.4	0.00	0.50	0.50	AgZr
				0.04	0.91	0.05	(Ag)
4#	0.10	0.79	0.11	0.30	0.21	0.49	τ_3
				0.09	0.84	0.07	(Ag)
5#	0.10	0.10	0.80	0.03	0.02	0.95	(αZr)
				0.03	0.30	0.67	$AgZr_2$
				0.23	0.02	0.75	$AlZr_3$
6#	0.19	0.76	0.05	0.15	0.81	0.04	(Ag)
				0.55	0.11	0.34	τ_2
7#	0.28	0.45	0.27	0.54	0.11	0.35	τ_2
				0.31	0.20	0.49	τ_3
				0.10	0.85	0.05	(Ag)
8#	0.38	0.54	0.08	0.59	0.14	0.27	τ_1
				0.33	0.67	0.00	Ag_2Al
9#	0.41	0.29	0.30	0.55	0.10	0.34	τ_2
				0.32	0.19	0.49	τ_3
				0.07	0.86	0.07	(Ag)
10#	0.41	0.41	0.18	0.55	0.11	0.34	τ_2
				0.20	0.80	0.00	(Ag)
				0.59	0.14	0.27	τ_1
11#	0.44	0.10	0.46	0.34	0.16	0.50	τ_3
				0.55	0.11	0.34	τ_2
				0.49	0.01	0.50	AlZr
12#	0.49	0.25	0.26	0.54	0.11	0.35	τ_2
				0.20	0.80	0.00	(Ag)
				0.58	0.14	0.28	τ_1
13#	0.58	0.20	0.22	0.35	0.65	0.00	Ag_2Al
				0.60	0.13	0.27	τ_1
14#	0.64	0.23	0.13	0.39	0.61	0.00	Ag_2Al
				0.73	0.00	0.27	Al_3Zr
				0.88	0.12	0.00	(Al)
15#	0.92	0.04	0.04	0.73	0.00	0.27	Al_3Zr
				0.95	0.05	0.00	(Al)

using TEM (Tecnai G^2 G20 ST) operating at 200 kV. The vacuum of the TEM was between 10^{-4} and 10^{-6} Torr.

Hardness testing

The hardness values of the τ_1 and τ_2 phases were measured on a nano-indenter (Anton-Paar NHT^2) with a Berkovich diamond indenter, and the indentation depth was maintained at 1 μm.

Calculation methods

Thermodynamic modeling

The Gibbs energy of a pure element is dependent on temperature and pressure. The molar enthalpy of stable elements at 298.15 K and 1 bar is commonly used as the standard element reference (SER) state. The Gibbs energy for the element *i* (*i* = Ag, Al, Zr) can be expressed as follows:

$$
{}^{0}G_{i}^{\varphi}(T) = a + b \cdot T + c \cdot T \cdot \ln T + d \cdot T^{2} + e \cdot T^{-1} + f \cdot T^{3} + g \cdot T^{7} + h \cdot T^{-9}
$$

The European Thermochemical Research Group (SGTE) has optimized the expressions of Gibbs energy as a function of temperature for all pure elements and established a corresponding database of lattice stability parameters. The Gibbs free energies for pure elements were retrieved from the Dinsdale compilation [43].

The solution phase φ (φ = Fcc_A1, Bcc_A2, Hcp_A3 and Liquid) is described using the substitutional solution model. Their Gibbs energy function is expressed by the following equation:

$$
G_{m}^{\varphi} - H^{SER} = \sum_{i=1}^{n} x_{i}{}^{0}G_{i}^{\varphi} + RT\sum_{i=1}^{n} x_{i}\ln(x_{i}) + {}^{ex}G^{\varphi}
$$

in which H^{SER} is the abbreviation of $x_{\mathrm{Al}} \cdot H_{\mathrm{Al}}^{\mathrm{SER}} + x_{\mathrm{Ag}} \cdot H_{\mathrm{Ag}}^{\mathrm{SER}} + x_{\mathrm{Zr}} \cdot H_{\mathrm{Zr}}^{\mathrm{SER}}$, and x_i is the mole fraction of component i (i = Al, Ag, Zr). ${}^{o}G_{i}^{\varphi}$ is the Gibbs energy for pure element i in the phase φ. R is the gas constant. ${}^{ex}G^{\varphi}$ is the excess Gibbs energy of the phase φ, which is described by the Redlich–Kister polynomial [44]:

$$
\begin{aligned}
{}^{ex}G^{\varphi} ={}& x_{Al}x_{Ag}\sum^{n} {}^{n}L_{Al,Ag}^{\varphi}(x_{Al} - x_{Ag})^{n} \\
&+ x_{Al}x_{Zr}\sum^{n} {}^{n}L_{Al,Zr}^{\varphi}(x_{Al} - x_{Zr})^{n} \\
&+_{Ag} x_{Zr}\sum^{n} {}^{n}L_{Ag,Zr}^{\varphi}(x_{Ag} - x_{Zr})^{n} \\
&+ x_{Al}x_{Ag}x_{Zr}L_{Al,Ag,Zr}^{\varphi}
\end{aligned}
$$

$$
L^{\varphi} = a + b \cdot T + c \cdot T \cdot \ln T + d \cdot T^{2} + e \cdot T^{-1} + \cdots
$$

$$
L_{Ag,Al,Zr}^{\varphi} = x_{Ag}{}^{0}L_{Ag,Al,Zr}^{\varphi} + x_{Al}{}^{1}L_{Ag,Al,Zr}^{\varphi} + x_{Zr}{}^{2}L_{Ag,Al,Zr}^{\varphi}
$$

where $L_{i,j}^{\varphi}$ (i, j = Al, Ag, Zr, and $i \neq j$) represent the nth binary interaction parameters between i with j, $L_{Ag,Al,Zr}^{\varphi}$ is the ternary interaction parameter to be evaluated in the present work.

The ternary intermetallic compound τ_1 is modeled as a stoichiometric phase. The Gibbs energy of each compound is given by the following expression:

$$
\begin{aligned}
&{}^{o}G_{m}^{Al_{x}Ag_{y}Zr_{z}} - x_{Al} \cdot H_{Al}^{SER} - y_{Ag} \cdot H_{Ag}^{SER} - z_{Zr} \cdot H_{Zr}^{SER} \\
&= A + B \cdot T + x_{Al}^{o}G_{Al}^{fcc} + y_{Ag}^{o}G_{Ag}^{fcc} + z_{Zr}^{o}G_{Zr}^{hcp}
\end{aligned}
$$

in which A and B are to be evaluated.

For the τ_2 and τ_3 phases, experimental results suggest that Ag may predominately replace Al. Therefore, the $(\mathrm{Al, Ag})_{1.84}(\mathrm{Ag})_{0.16}(\mathrm{Zr})_{1}$ and $(\mathrm{Al, Ag})_{6}(\mathrm{Ag})_{1}(\mathrm{Zr})_{6}$ thermodynamic models are employed to describe phases τ_2 and τ_3, respectively. The Gibbs energy of these phases can be expressed as follows:

$$
\begin{aligned}
{}^{o}G_{m}^{(Al,Ag)_{x}Ag_{y}Zr_{z}} ={}& y_{Al}^{'}G_{Al:Ag:Zr}^{\varphi} + y_{Ag}^{'}G_{Ag:Ag:Zr}^{\varphi} \\
&+ xRT\left(y_{Al}^{'}\ln y_{Al}^{'} + y_{Ag}^{'}\ln y_{Ag}^{'}\right) \\
&+ y_{Al}^{'}y_{Ag}^{'}{}^{o}L_{Al,Ag:Ag:Zr}^{\varphi}
\end{aligned}
$$

where x, y, z denote the number of sites in each sublattice, and $y_{Al}^{'}$ and $y_{Ag}^{'}$ represent the site fractions of Al and Ag on the first sublattice. $G_{Al:Ag:Zr}^{\varphi}$ and $G_{Ag:Ag:Zr}^{\varphi}$ are the molar Gibbs energies of the end-members. ${}^{o}L_{Al,Ag:Ag:Zr}^{\varphi}$ represent the interaction parameters between Al and Ag in the first sublattice, expressed by the Redlich–Kister polynomials.

First-principles calculation

The formation enthalpies of ternary compounds τ_1, τ_2, τ_3 and the binary compounds with solid solubility were computed by the Vienna ab-initio simulation package (VASP) [45], based on density functional theory (DFT). The computational details can be found in our previous work [14]. The formation enthalpy $\Delta H_f(Al_xZr_y)$ at 0 K could be expressed by the following equation:

$$
\Delta \mathrm{H_f}\left(\mathrm{Al_xZr_y}\right) = \mathrm{E}\left(\mathrm{Al_xZr_y}\right) - [\mathrm{x_{Al}E(Al)} + \mathrm{x_{Zr}E(Zr)}]
$$

where $\mathrm{E(Al_xZr_y)}$ is the calculated total energy of the structure $\mathrm{Ag_xZr_y}$, and E(Al) and E(Zr) denote the total energies of $\mathrm{Al_xZr_y}$, fcc-Al and hcp-Zr at 0 K, respectively. $\mathrm{x_i}$ (i = Al or Zr) is the atomic fraction of the component i.

The enthalpy of formation for the ternary compound can be defined as:

$$
\Delta \mathrm{H_f}\left(\mathrm{Al_xAg_yZr_z}\right) = \left[\mathrm{E}\left(\mathrm{Al_xAg_yZr_z}\right) - \mathrm{x_{Al}E(Al)} - \mathrm{y_{Ag}E(Ag)} - \mathrm{z_{Zr}E(Zr)}\right]
$$

in which, $\mathrm{E(Al_xAg_yZr_z)}$, E(Al), E(Ag), E(Zr) are the total energies of $\mathrm{Al_xAg_yZr_z}$, fcc-Al, fcc-Ag and hcp-Zr, respectively, at 0 K.

Results and discussion

Establishing a thermodynamic database of the Al–Ag–Zr System

Tables 2 and 3 summarize the experimental results of phase composition measurements of alloy samples annealed at 500 °C for 120 days and 600 °C for 90 days. The isothermal sections of the Al–Ag–Zr system at 500 and 600 °C were obtained based on these experimental results, combined with the first-principles calculations of the formation enthalpy of τ_1, τ_2, τ_3, and some metastable end-members phases. The thermodynamic optimization of Al–Ag–Zr system was performed using the PARROT module incorporated in Thermo-Calc software [34]. The optimized parameters are shown in Table 5.

Table 3 Equilibrium phase constitution and compositions of the constituent phases measured in the annealed Al–Ag–Zr alloys at 600 °C

Alloy no	Nominal composition (at.)			EPMA analyzed composition (at.)			Phase determination
	Al	Ag	Zr	Al	Ag	Zr	
1#	0.01	0.02	0.97	0.01	0.02	0.97	(αZr)
2#	0.02	0.18	0.8	0.03	0.03	0.94	(αZr)
				0.01	0.32	0.67	$AgZr_2$
3#	0.02	0.58	0.4	0.00	0.51	0.49	AgZr
				0.05	0.90	0.05	(Ag)
4#	0.10	0.79	0.11	0.33	0.17	0.50	τ_3
				0.06	0.90	0.04	(Ag)
5#	0.10	0.10	0.80	0.04	0.02	0.94	(αZr)
				0.02	0.30	0.68	$AgZr_2$
				0.22	0.02	0.76	$AlZr_3$
6#	0.19	0.76	0.05	0.11	0.89	0.00	(Ag)
				0.57	0.19	0.24	τ_1
				0.55	0.11	0.34	τ_2
7#	0.28	0.45	0.27	0.55	0.11	0.34	τ_2
				0.34	0.16	0.50	τ_3
				0.09	0.88	0.03	(Ag)
8#	0.38	0.54	0.08	0.58	0.17	0.25	τ_1
				0.27	0.73	0.00	Ag_2Al
9#	0.41	0.29	0.30	0.55	0.11	0.34	τ_2
				0.34	0.16	0.50	τ_3
				0.09	0.88	0.03	(Ag)
10#	0.41	0.41	0.18	0.10	0.90	0.00	(Ag)
				0.58	0.18	0.24	τ_1
				0.55	0.11	0.34	τ_2
11#	0.44	0.10	0.46	0.37	0.13	0.50	τ_3
				0.55	0.11	0.34	τ_2
				0.49	0.02	0.49	AlZr
12#	0.49	0.25	0.26	0.11	0.89	0.00	(Ag)
				0.57	0.19	0.24	τ_1
				0.55	0.11	0.34	τ_2
13#	0.58	0.20	0.22	0.58	0.18	0.24	τ_1
				0.31	0.00	0.69	Ag_2Al
14#	0.64	0.23	0.13	0.39	0.61	0.00	Ag_2Al
				0.72	0.01	0.27	Al_3Zr
				0.61	0.39	0.00	Liquid
15#	0.92	0.04	0.04	0.73	0.00	0.27	Al_3Zr
				0.95	0.05	0.00	(Al)

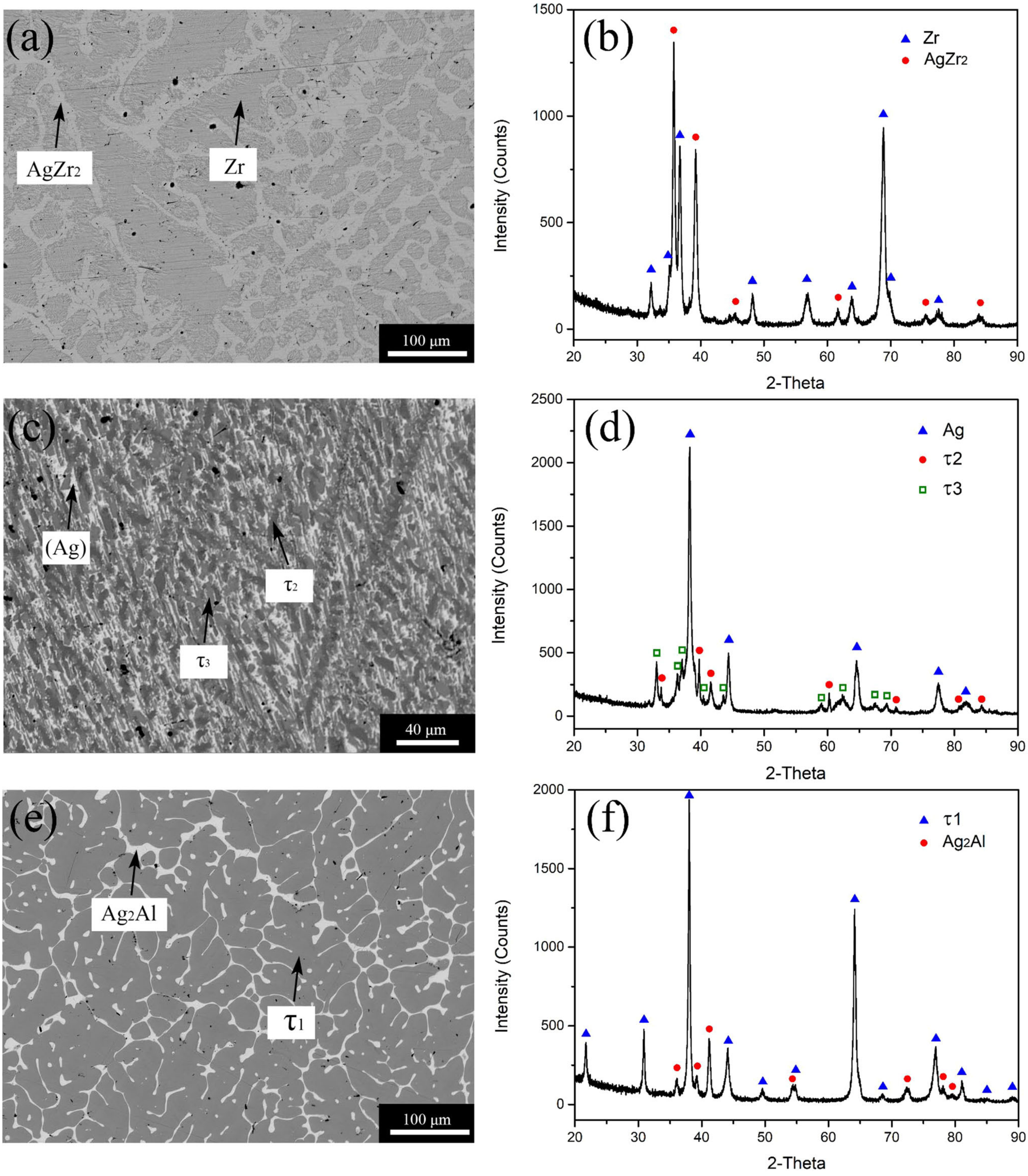

Figure 2 BEI (**a**, **c**, **e**) and XRD patterns (**b**, **d**, **f**) of alloys 2#, 7#, and 8# after annealing at 500 °C for 120 days.

Representative alloys located in different phase regions are discussed. As shown in Fig. 2a, two phases can be observed in 2#. According to the results of the EPMA and XRD, the dark and bright phases are $AgZr_2$ and Zr, respectively. In addition, the eutectic structure of $AgZr_2$ and Zr can be observed in

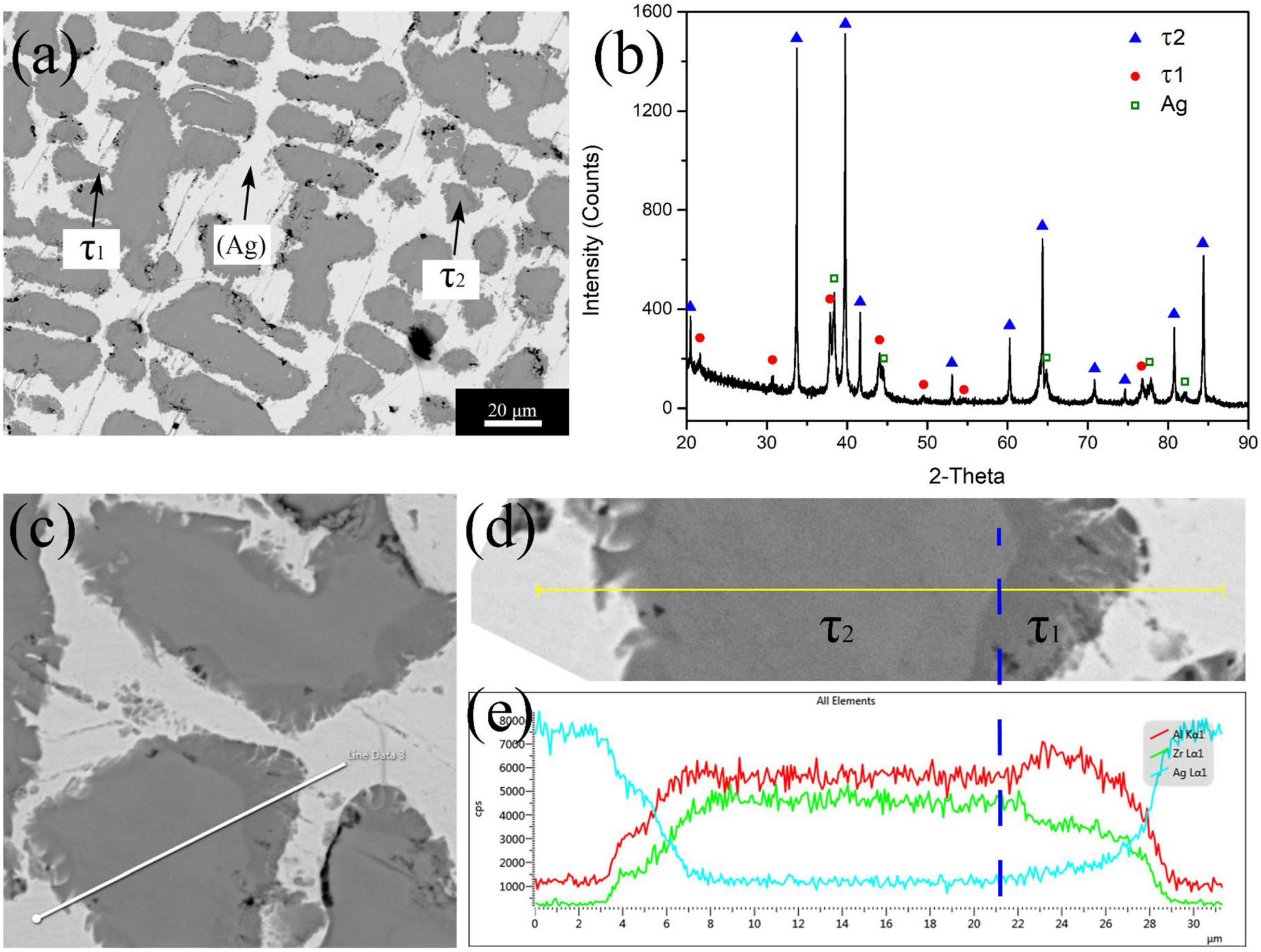

Figure 3 BEI image (**a**) and XRD pattern (**b**) of alloy 10# after annealing at 500 °C for 120 days. (**c**), (**d**), and (**e**) show the line scan results of the 10# at high magnification, where the lighter phase in (**d**) represents τ_2, and the darker phase represents τ_1.

this sample. Similarly, 7# and 8# exhibit a three-phase equilibrium of $\tau_2 + \tau_3 + (\mathrm{Ag})$ and a two-phase equilibrium of $Ag_2Al + \tau_1$. Some samples exhibit unevenly distributed black spots on the surface, which may be attributed to inherent pores in the samples or to water stains and contaminants introduced during the polishing and cleaning processes.

The microstructure of alloy 10# is shown in Fig. 3a. Notably, the dark τ_2 phase is covered by a layer of τ_1 phase, which is true for each grain. The microstructure of 10# is shown at higher magnification in Fig. 3c. The lighter phase is evidently encompassed by the darker phase, resulting in a structure similar to that of a core–shell. The line scan analysis in Fig. 3e exhibits significant changes in composition at the interface of two different contrasts. Combined with the XRD result, we determined that 10# is located in the three-phase region of $(\mathrm{Ag}) + \tau_1 + \tau_2$, and this interesting phenomenon will be further studied in future.

As illustrated in Fig. 4a, 14# is in a three-phase equilibrium, where the plate-like phase is Al_3Zr, the light phase is Ag_2Al, and the darker phase is (Al). For 15#, as shown in Fig. 4c, the matrix phase is (Al), and the plate-like phase is Al_3Zr. The XRD results of 14# and 15# confirm that they form phase equilibria as

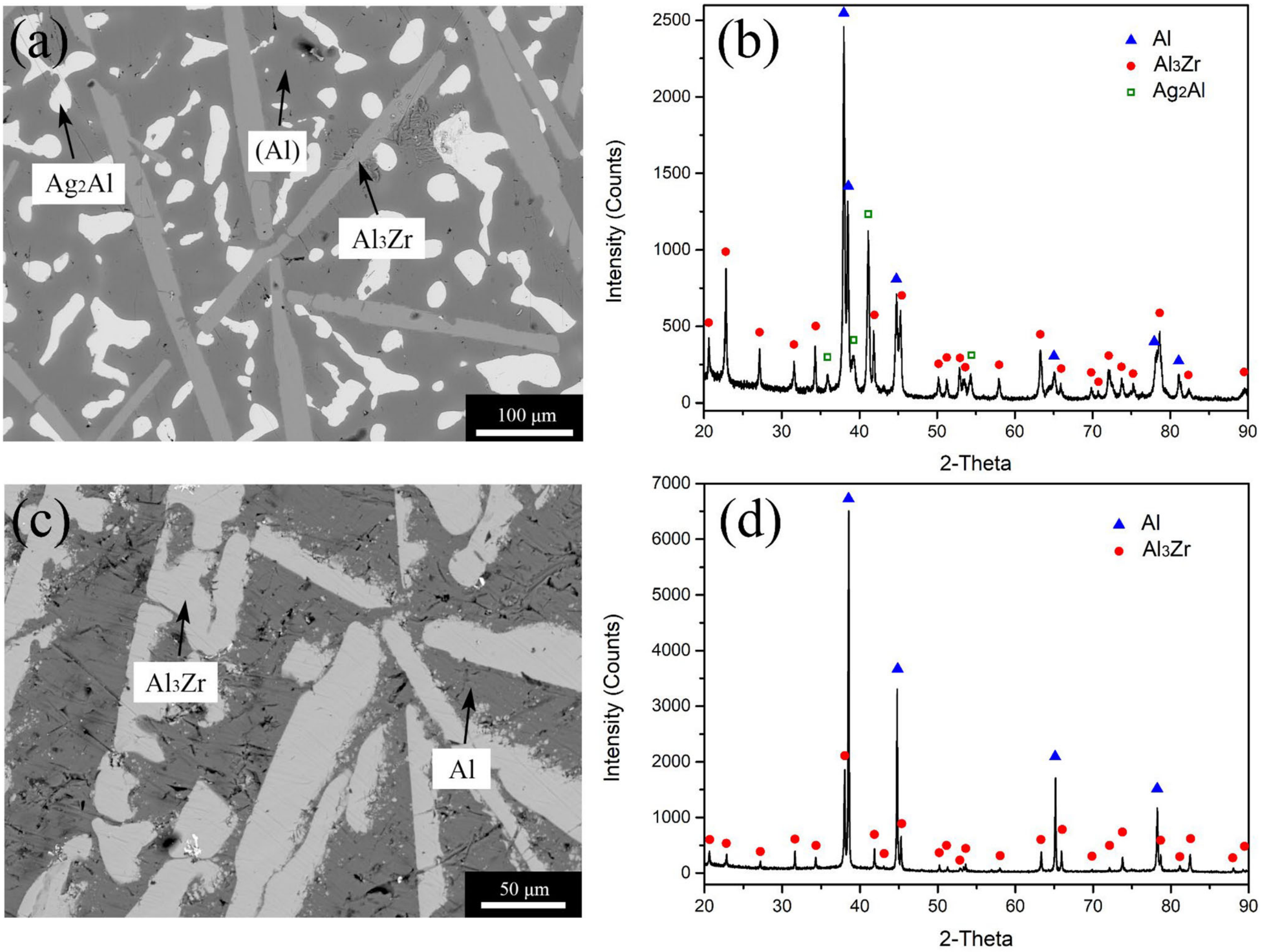

Figure 4 BEI images (**a**, **c**) and XRD patterns (**b**, **d**) of alloys 14# and 15# after annealing at 500 °C for 120 days.

Ag_2Al + (Al) + Al_3Zr and Al_3Zr + (Al), respectively.

Figure 5 presents the XRD results of 3#, 5#, and 6#. The diffraction peaks of the samples match well with the corresponding phases. After annealing for an extended period, alloys 3#, 5#, and 6# form phase equilibria of AgZr + (Ag), (αZr) + Al_3Zr + Ag_2Zr, and (Ag) + τ_2, respectively.

Table 2 summarizes the phase equilibria formed by alloy samples with different compositions after annealing at 500 °C for 120 days. Combined with the evaluation of the studies by Kotur et al. [17] and Hsiao et al. [18], the isothermal section of the Al–Ag–Zr system at 500 °C is constructed, as shown in Fig. 6. The experimental results reveal the presence of five three-phase regions: Al_3Zr + Ag_2Al + (Al), $\tau_1 + \tau_2$ + (Ag), $\tau_2 + \tau_3$ + (Ag), AlZr + $\tau_2 + \tau_3$, and (αZr) + $AlZr_3$ + $AgZr_2$ and six two-phase regions: Al_3Zr + (Al), $Ag_2Al + \tau_1$, τ_2 + (Ag), τ_3 + (Ag), AgZr + (Ag), and (Zr) + $AgZr_2$.

Figure 7 shows the Backscattered electron image (BEI) and XRD results of 4#, 8# and 10#. The microstructure of 4# is shown in 4a, the dark lath-like phase in 4a is determined to be τ_3 by EPMA and XRD

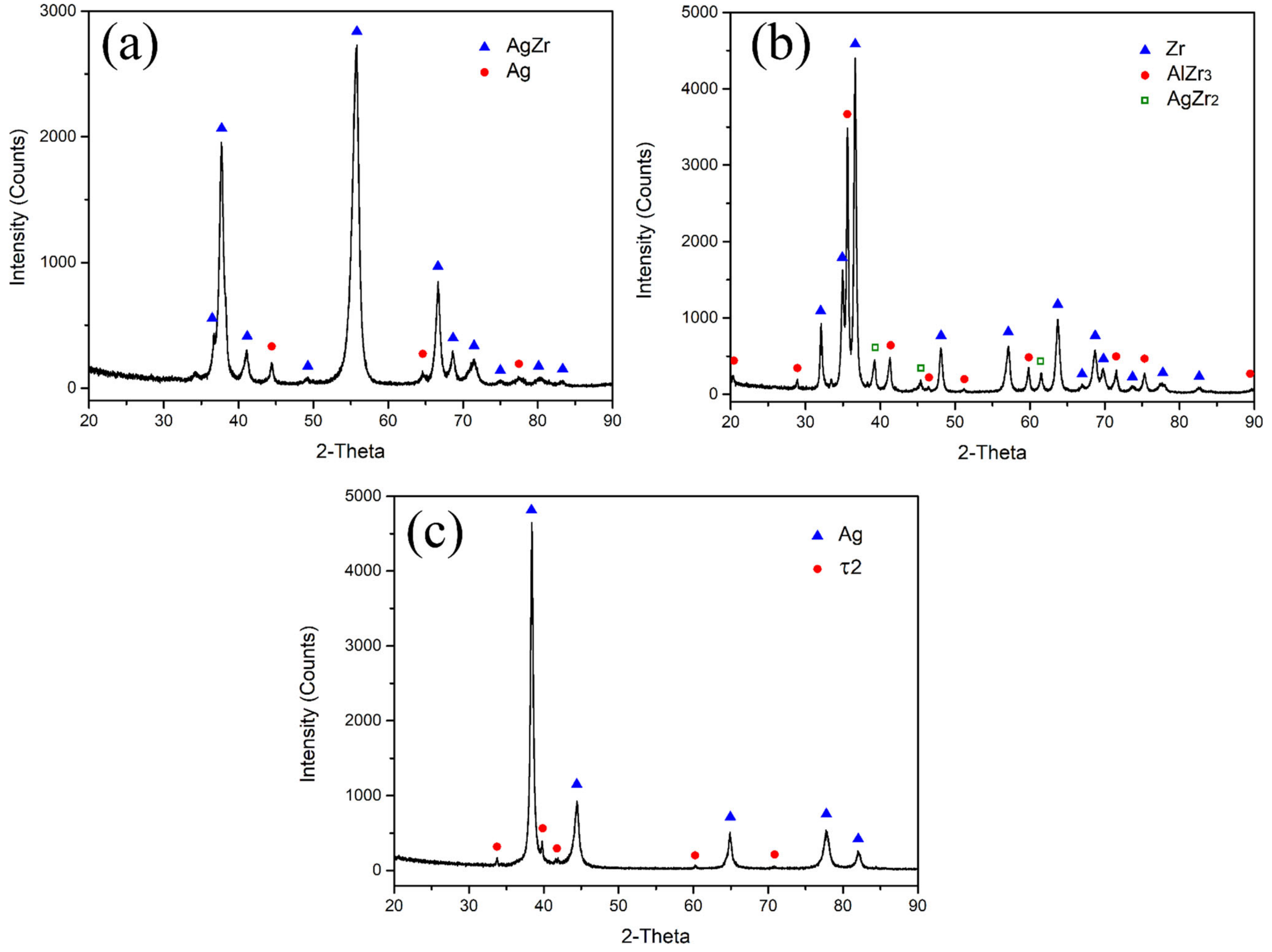

Figure 5 XRD patterns (**a**, **b**, **c**) of alloys 3#, 5#, and 6# after annealing at 500 °C for 120 days.

whereas the light area corresponds to the (Ag) phase. For 8#, as shown in 4c, the dark phase with large area is τ_1, and the light phase is Ag_2Al, which is in good agreement with the XRD results. The results for 10# are similar to the result at 500 °C, located in the three-phase region of (Ag) + τ_1 + τ_2.

The XRD results of 2#, 3#, 5#, and 6# annealing at 600 °C for 90 days are shown in Fig. 8, and all diffraction peaks correspond well to the corresponding phases. These samples form the phase equilibria of (αZr) + $AgZr_2$, AgZr + (Ag), (αZr) + Al_3Zr + Ag_2Zr, and (Al) + Al_3Zr, respectively.

Similarly, we measured the isothermal section of the Al–Ag–Zr system at 600 °C, which include five three-phase regions and five two-phase regions, as shown in Fig. 9. Except for the appearance of an Al-rich end liquid phase, resulting from the melting of Al at 600 °C, the results elsewhere are similar to those at 500 °C.

Identification of the τ_3 phase and determination of its equilibrium with neighboring phases

The microstructure of 4# after long-time annealing at 500 and 600 °C is shown in Fig. 10a and b. EPMA analysis determined that the light phase is (Ag), whereas the dark phase, with a composition of

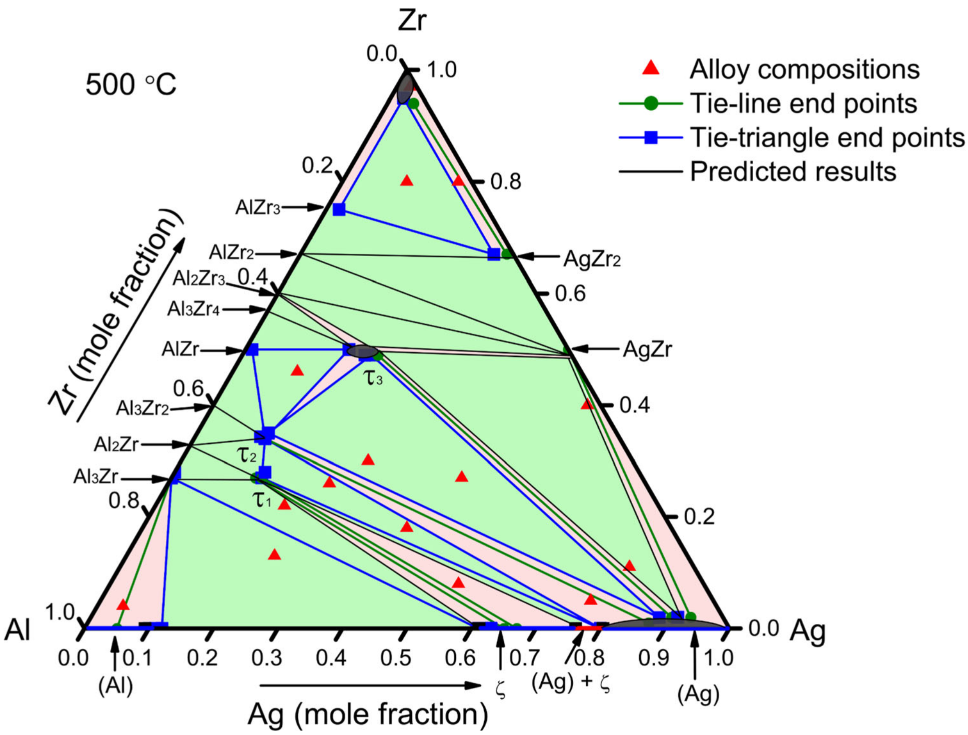

Figure 6 The experimental isothermal section of the Al–Ag–Zr system at 500 °C. The data shown for end points are experimentally measured compositions.

Al:Ag:Zr close to 0.33:0.17:0.50, corresponds to τ_3. This conclusion is supported by the XRD patterns in Fig. 10c. The TEM bright-field phase of 4# after annealing at 600 °C for 90 days is presented in Fig. 10d, with the corresponding selected area electron diffraction (SAED) patterns shown in Fig. 10e and f for regions 1 and 2, respectively. After identification, the grain in the middle of Fig. 10d was determined to be τ_3, while the grains on the left and right sides were determined to be (Ag). Therefore, we demonstrate that the phase with composition Al: Ag: Zr close to 0.33: 0.17: 0.50 is τ_3, rather than Al_3Zr_4.

The correct phase relationship serves as the foundation for constructing a thermodynamic database, and a self-consistent thermodynamic database can guide material design. Therefore, we determined τ_3 + AgZr + (Ag) three-phase equilibrium instead of Al_3Zr_4 + AgZr + (Ag) in the isothermal section. To prove that the three-phase region existing at 500 and 600 °C is τ_3 + AgZr + (Ag) instead of Al_3Zr_4 + AgZr + (Ag) as proposed by Kotur et al. [17] and Hsiao et al. [18], we additionally prepared two samples with the same composition as 11# and 12# in the study by Hsiao et al. Figure 11a and c shows the as-cast microstructure of 16# and 17#, respectively, in which the dark strip phase correspond to τ_3. The EPMA results are shown in Table 4. The XRD results in Fig. 11b and d also confirm that the specimens were located in the three-phase region of τ_3 + AgZr + (Ag), which is consistent with our calculated results. In the report by Hsiao et al. [18], the XRD results of 10#, 11# and 12# were not given, and their EPMA results showed that Ag has a large solid solution in the Al_3Zr_4 phase, which is close to the composition of the τ_3 phase we measured. Therefore, we consider the three-phase equilibrium to be τ_3 + AgZr + (Ag).

Additionally, we prepared alloy sample 18# with a composition of $Al_{0.42}Ag_{0.06}Zr_{0.52}$. Through XRD and EPMA analysis, the sample was found to be in the three-phase region of Al_3Zr_4 + τ_3 + AlZr, directly confirming the existence of τ_3 as a separate phase from Al_3Zr_4 and further validating the accuracy of our experimental phase diagram.

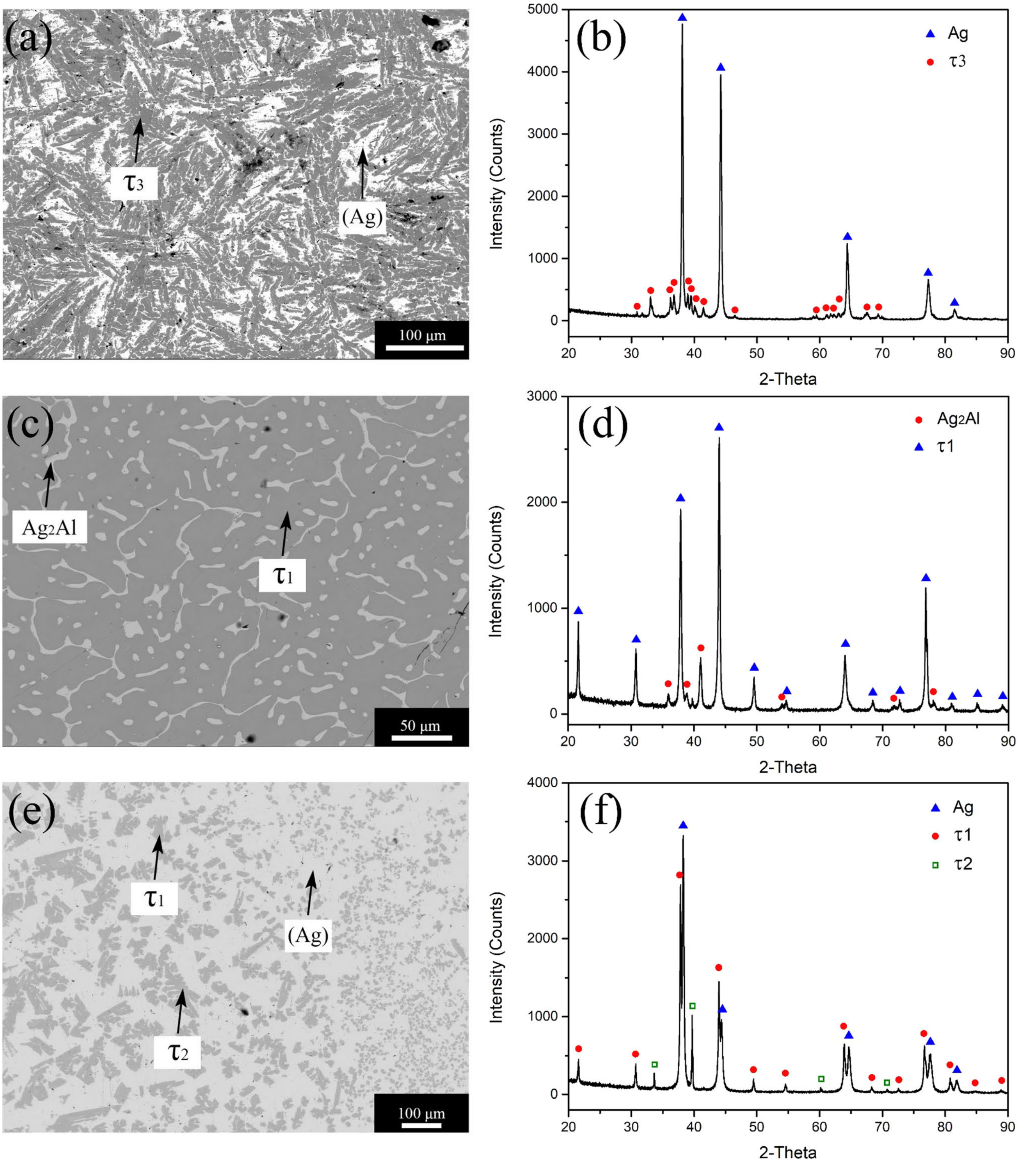

Figure 7 BEI images (**a**, **c**, **e**) and XRD patterns (**b**, **d**, **f**) of alloys 4#, 8#, and 10#, respectively, after annealing at 600 °C for 90 days.

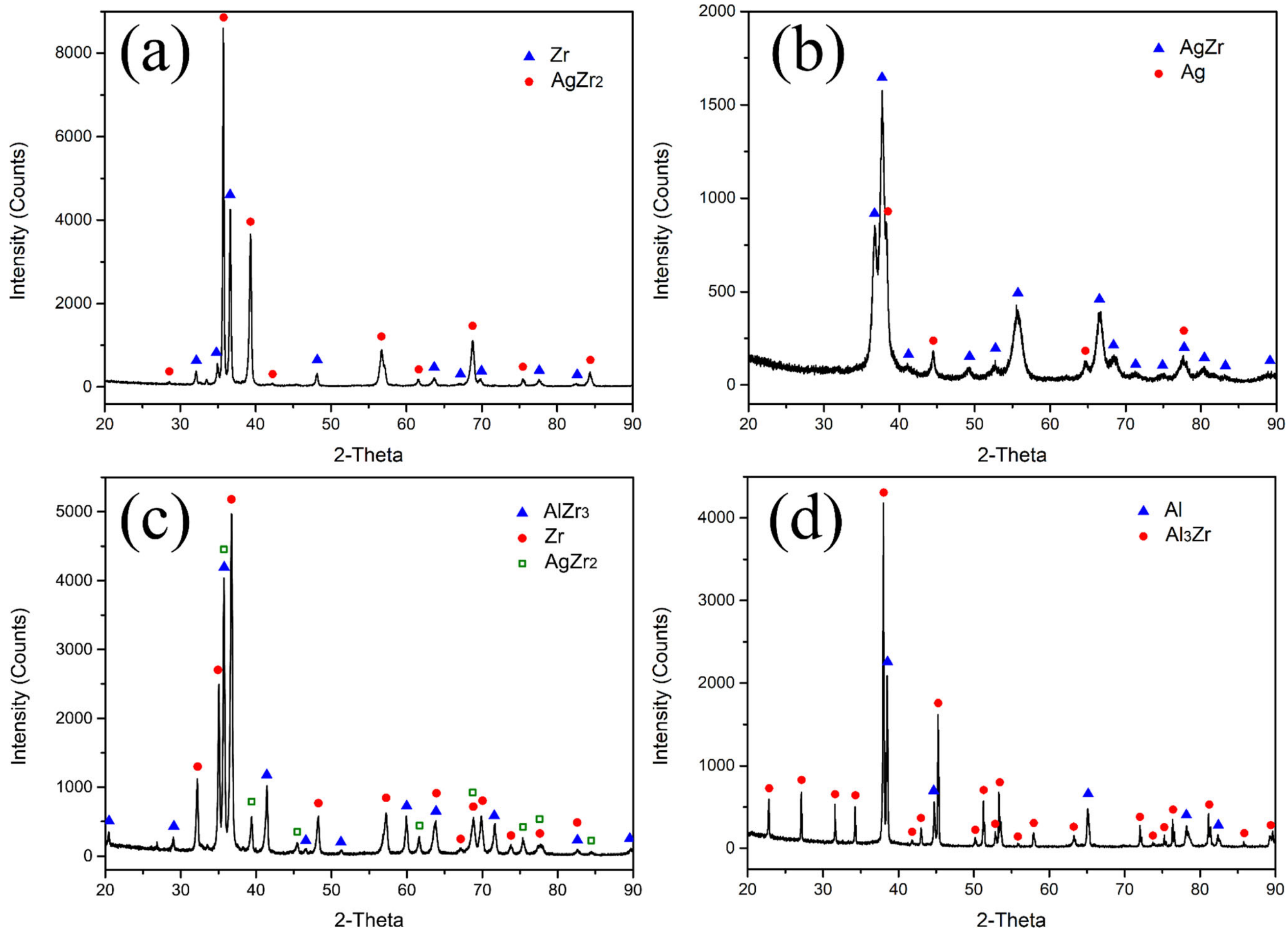

Figure 8 XRD patterns (**a**, **b**, **d**, **f**) of alloys 2#, 3#, 5#, and 15#, respectively, after annealing at 600 °C for 90 days.

First-principles calculation and thermodynamic optimization

Through the analysis of the experimental results, we determined the solid solubility of some phase in the Al–Ag–Zr system and provided its corresponding thermodynamic models. First-principles calculations were incorporated to compute the zero-Kelvin energies of end-member phases in unstable structures, because experimental data are not available for these phases. The energies of the ternary phases τ_1, τ_2, and τ_3, whose crystal structures are known, were calculated. The results of the first-principles calculations are shown in Table 5.

The constituent Al–Ag, Al–Zr, and Ag–Zr binary system were taken from the reports by Witusiewicz et al. [19], Fischer et al. [20], and Hsiao et al. [26], respectively. With the precise descriptions for the boundary binary systems, the phase equilibria and thermodynamic properties in the Al–Ag–Zr ternary system were computed via the standard procedure. The optimization procedures were conducted in the program PARROT module embedded in Thermo-Calc software [34] using the step-by-step optimization method reported by Du et al. [46]. Table 6 summarizes the optimized thermodynamic parameters of this ternary system.

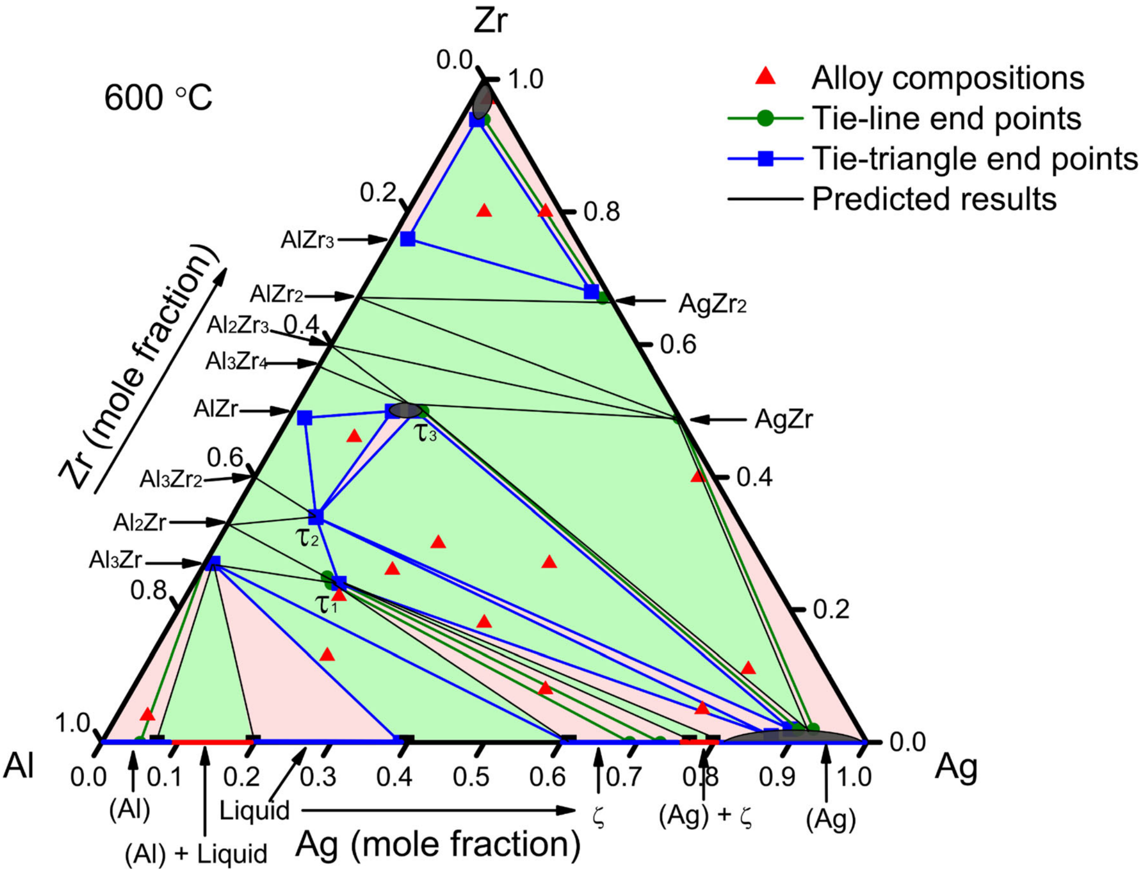

Figure 9 The experimental isothermal section of the Al–Ag–Zr system at 600 °C. The data shown for end points are experimentally measured compositions.

As seen in Fig. 12a, the calculated results agree well with our experimental results and those of previous reports. Notably, we have confirmed that the three-phase equilibrium is τ_3 + AgZr + (Ag) rather than Al_3Zr_4 + AgZr + (Ag). In Fig. 12b, the calculated isothermal section at 600 °C is also consistent with our experimental results, and all phase equilibria are accurately represented. It is worth noting that, in order to ensure the consistency between the calculated isothermal sections at 500 and 600 °C and the experimental data, we sacrificed the solid solubility of some phases, such as $AgZr_2$ and AgZr, within a reasonable error range. We have therefore established a self-consistent and reliable Al–Ag–Zr thermodynamic database for alloy design.

The liquidus projection of the Al–Ag–Zr system is presented in Fig. 13, where all primary phases and isothermal lines are labeled. To better understand the solidification path and liquidus surface, we have calculated a partial Scheil reaction scheme for the Al–Ag–Zr system (Fig. 14) using the database obtained in this study. The scheme includes seven critical reactions.

High-strength ternary phase τ_2 in Al–Ag–Zr system

To investigate the influence on the properties of the alloy of the two ternary phases, τ_1 and τ_2, located at the Al-rich end in the Al–Ag–Zr system, the hardness of τ_1 and τ_2 was measured using a nanoindentation

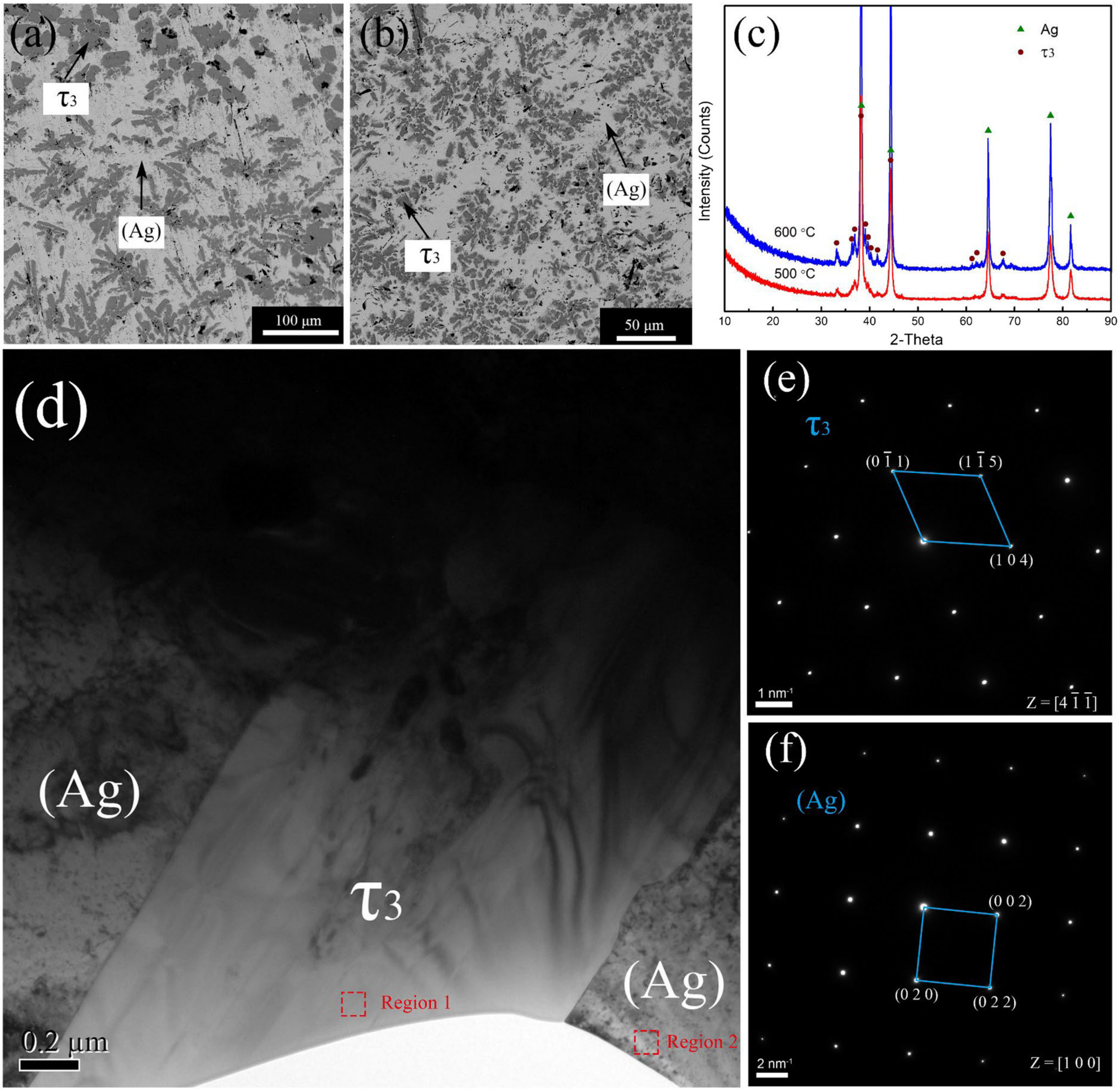

Figure 10 (**a**) and (**b**) Microstructures of 4# after annealing at 500 and 600 °C, respectively, and (**c**) XRD results. (**d**) TEM bright-field image of 4# after annealing at 600 °C, with (Ag) on both sides and a τ_3 phase in the middle. (**e**) and (**f**) Diffraction patterns corresponding to regions 1 and 2 in (**d**).

instrument. The microstructure of the sample is presented in Fig. 15a and b, and the residual imprints of the indentation are indicated with red circles in Fig. 15c and d. The indentation measurements performed on the single phases of τ_1 and τ_2, respectively, were repeated three times, and the average value of three consistent measurements was taken as the hardness of the single phase. The results are shown in Table 6. The load–displacement curves corresponding to τ_1 and τ_2 are shown in Fig. 15e.

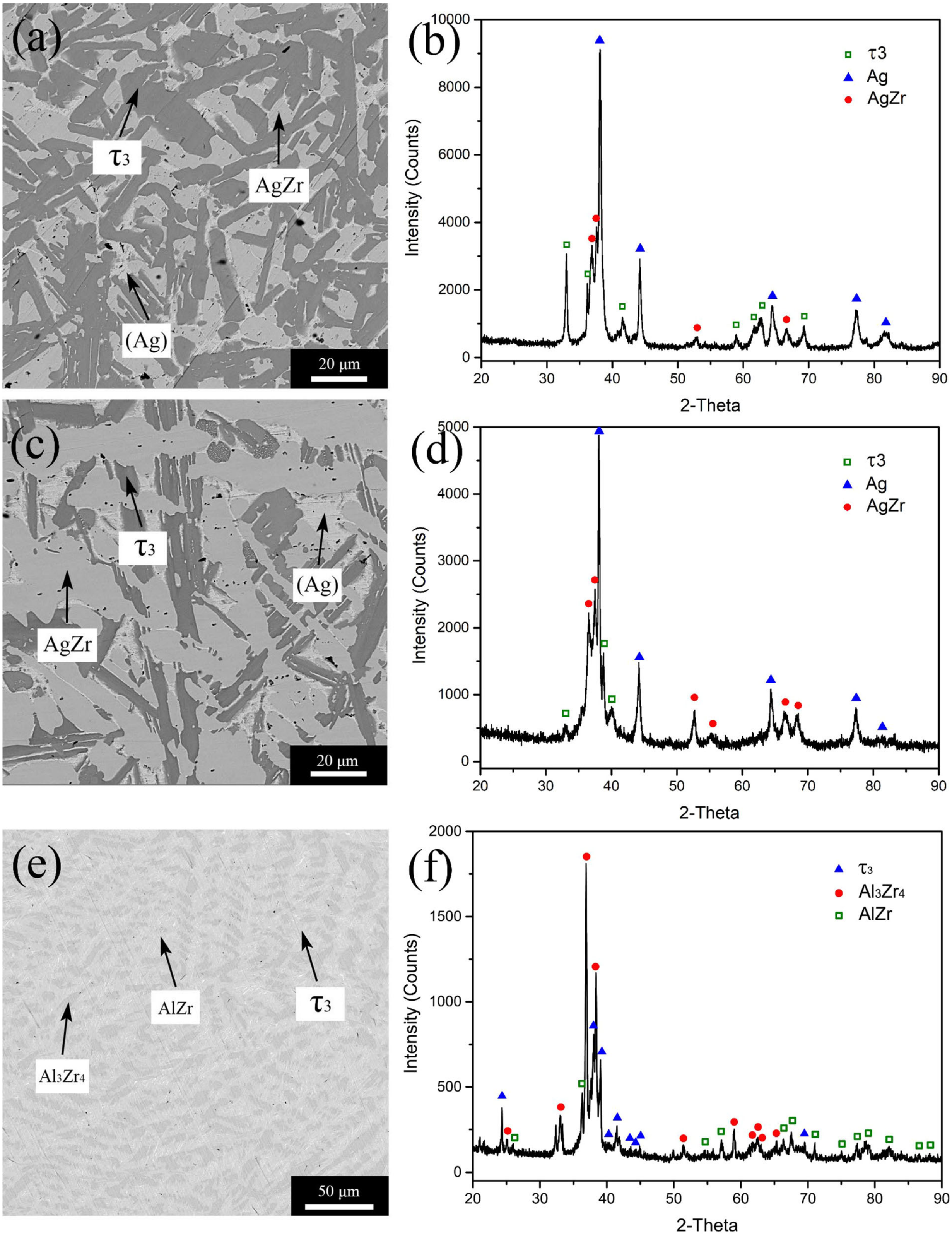

Figure 11 BEI images (**a**, **c**, **e**) and XRD patterns (**b**, **d**, **f**) of 16#, 17#, and 18#, respectively.

Table 4 The phase constitution and measured compositions of constituent phases

Alloy No.	Nominal composition (at.)			EPMA analyzed composition (at.)			Phase determination
	Al	Ag	Zr	Al	Ag	Zr	
16#	0.20	0.40	0.40	0.32	0.18	0.50	τ_3
				0.02	0.48	0.50	AgZr
				0.01	0.04	0.95	(Ag)
17#	0.10	0.50	0.40	0.29	0.17	0.54	τ_3
				0.01	0.49	0.50	AgZr
				0.00	0.01	0.99	(Ag)
18#	0.42	0.06	0.52	0.34	0.14	0.52	τ_3
				0.42	0.02	0.56	Al_3Zr_4
				0.44	0.08	0.48	AlZr

Table 5 A summary of the results from the first-principles calculations kJ/(mole of atoms)

Phase	Model	Formula	First principles (0 K)
AgZr	$(Ag, Al)_1(Zr)_1$	AlZr	− 21.4
$AgZr_2$	$(Ag, Al)_1(Zr)_2$	$AlZr_2$	− 27.6
τ_1	$(Al)_{2.68}(Ag)_{0.32}(Zr)_1$	$Al_{2.68}Ag_{0.32}Zr$	− 45.3
τ_2	$(Al, Ag)_{1.84}(Ag)_{0.16}(Zr)_1$	$Al_{1.84}Ag_{0.16}Zr$	− 48.6
		$Ag_{1.84}Ag_{0.16}Zr$	+ 15.1
τ_3	$(Al, Ag)_6(Ag)_1(Zr)_6$	Al_6AgZr_6	− 43.2
		Ag_6AgZr_6	+ 1.6

Table 6 Summary of the thermodynamic parameters of the Al–Ag–Zr system in this work

Phase	Model	Thermodynamic parameters (J/mol)
Liquid	$(Ag, Al, Zr)_1$	${}^{0}L^{\mathrm{Liquid}}_{\mathrm{Ag,Al,Zr}} = -80{,}000$
Fcc_A1	$(Ag, Al, Zr)_1(Va)_1$	${}^{0}L^{\mathrm{Fcc\_A1}}_{\mathrm{Ag,Al,Zr:Va}} = -60{,}000$
AgZr	$(Ag, Al)_1(Zr)_1$	${}^{0}G^{\mathrm{AgZr}}_{\mathrm{Al:Zr}} - {}^{0}G^{\mathrm{fcc}}_{\mathrm{Al}} - {}^{0}G^{\mathrm{hcp}}_{\mathrm{Zr}} = -43{,}200$
		${}^{0}L^{\mathrm{AgZr}}_{\mathrm{(Ag,Al):Zr}} = -65{,}000$
$AgZr_2$	$(Ag, Al)_1(Zr)_2$	${}^{0}G^{\mathrm{AgZr_2}}_{\mathrm{Al:Zr}} - {}^{0}G^{\mathrm{fcc}}_{\mathrm{Al}} - 2 \cdot {}^{0}G^{\mathrm{hcp}}_{\mathrm{Zr}} = -82{,}800$
		${}^{0}L^{\mathrm{AgZr_2}}_{\mathrm{(Ag,Al):Zr}} = -30{,}000$
τ_1	$(Al)_{2.68}(Ag)_{0.32}(Zr)_1$	${}^{0}G^{\mathrm{Al_{2.68}Ag_{0.32}Zr}}_{\mathrm{Al:Ag:Zr}} - 2.68 \cdot {}^{0}G^{\mathrm{fcc}}_{\mathrm{Al}} - 0.32 \cdot {}^{0}G^{\mathrm{fcc}}_{\mathrm{Ag}} - {}^{0}G^{\mathrm{hcp}}_{\mathrm{Zr}} = -171{,}200$
τ_2	$(Al, Ag)_{1.84}(Ag)_{0.16}(Zr)_1$	${}^{0}G^{\mathrm{Al_{1.84}Ag_{0.16}Zr}}_{\mathrm{Al:Ag:Zr}} - 1.84 \cdot {}^{0}G^{\mathrm{fcc}}_{\mathrm{Al}} - 0.16 \cdot {}^{0}G^{\mathrm{fcc}}_{\mathrm{Ag}} - {}^{0}G^{\mathrm{hcp}}_{\mathrm{Zr}} = -140{,}800$
		${}^{0}G^{\mathrm{Al_{1.84}Ag_{0.16}Zr}}_{\mathrm{Ag:Ag:Zr}} - 2 \cdot {}^{0}G^{\mathrm{fcc}}_{\mathrm{Ag}} - {}^{0}G^{\mathrm{hcp}}_{\mathrm{Zr}} = -5000$
τ_3	$(Al, Ag)_6(Ag)_1(Zr)_6$	${}^{0}G^{\mathrm{Al_6AgSc_6}}_{\mathrm{Al:Ag:Sc}} - 6 \cdot {}^{0}G^{\mathrm{fcc}}_{\mathrm{Al}} - {}^{0}G^{\mathrm{fcc}}_{\mathrm{Ag}} - 6 \cdot {}^{0}G^{\mathrm{hcp}}_{\mathrm{Zr}} = -540{,}600$
		${}^{0}G^{\mathrm{Al_6AgSc_6}}_{\mathrm{Ag:Ag:Sc}} - 7 \cdot {}^{0}G^{\mathrm{fcc}}_{\mathrm{Ag}} - 6 \cdot {}^{0}G^{\mathrm{hcp}}_{\mathrm{Zr}} = -5000$

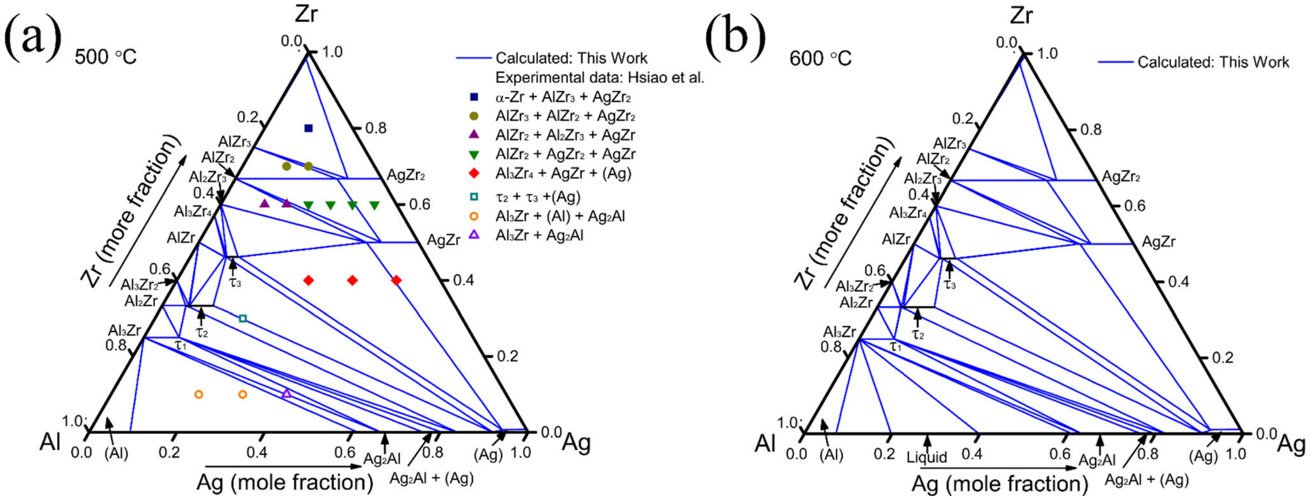

Figure 12 Calculated isothermal sections of the Al–Ag–Zr system at (**a**) 500 °C and (**b**) 600 °C compared with literature data.

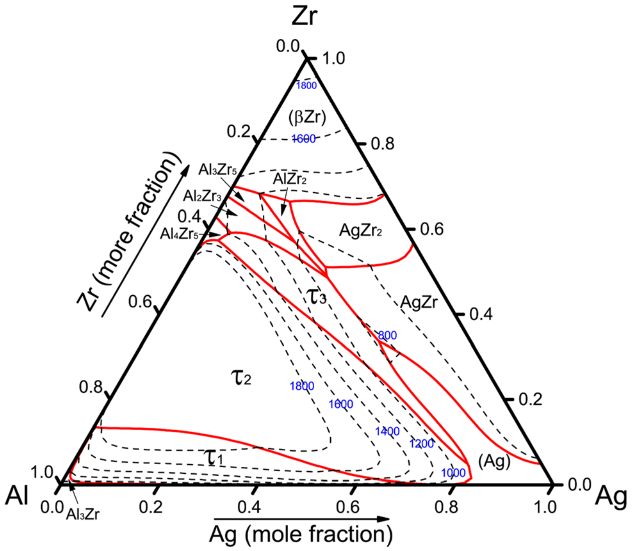

Figure 13 Calculated liquidus projection of the Al–Ag–Zr system.

According to the load–displacement curve, the average hardness values of τ_1 and τ_2 are 3.82 and 10.20 GPa, respectively. The hardness of τ_2 was much higher than that of τ_1 and exceeded that of the common strengthening Al_9FeNi (7.71 GPa at room temperature) in Al alloys. Therefore, in the design of Al alloys, the mechanical properties of the material can be significantly improved by introducing the strengthening phase τ_2 (Table 7).

Conclusions

In this work, we determined the isothermal sections of the Al–Ag–Zr system at 500 and 600 °C using the equilibrium alloy method. Six two-phase regions and five three-phase regions were identified at 500 °C, while five two-phase regions and five three-phase regions were identified at 600 °C. Additionally, we identified the uncertain τ_3 phase using TEM, and determined that the three-phase equilibrium at 500 and 600 °C consists of τ_3 + AgZr + (Ag), instead of Al_3Zr_4 + AgZr + (Ag). Based on our experimental results and first-principles calculations, we established a thermodynamic database for the Al–Ag–Zr system. Comparing it with previous literature data afforded, a good agreement between calculated and experimental results. Furthermore, we used nanoindentation to measure the hardness of the Al-rich ternary phases τ_1 and τ_2, which were found to have hardness values of 3.82 and 10.20 GPa, respectively. Therefore, introducing τ_2 as a strengthening phase in the design of Al alloys can significantly enhance their mechanical performance.

Figure 14 The partial Scheil reaction scheme of the Al–Ag–Zr system according to the present calculations (Temperature in °C).

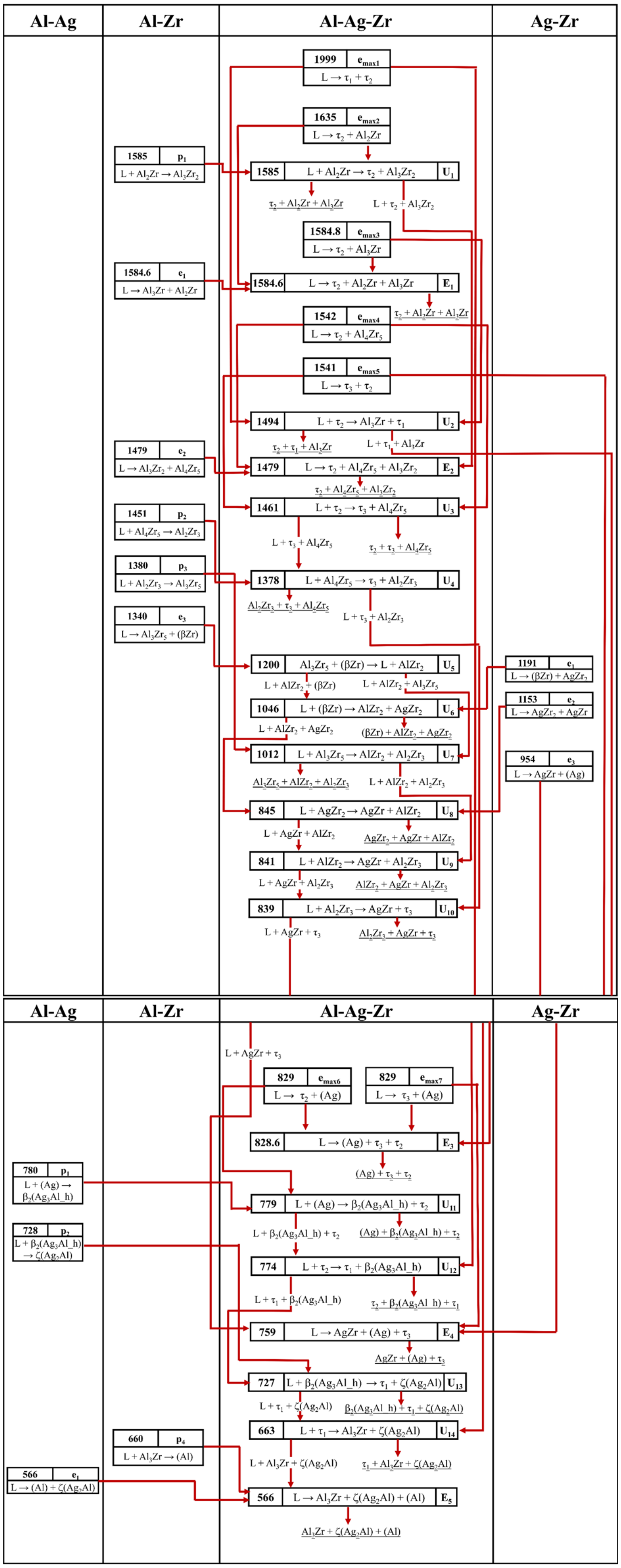

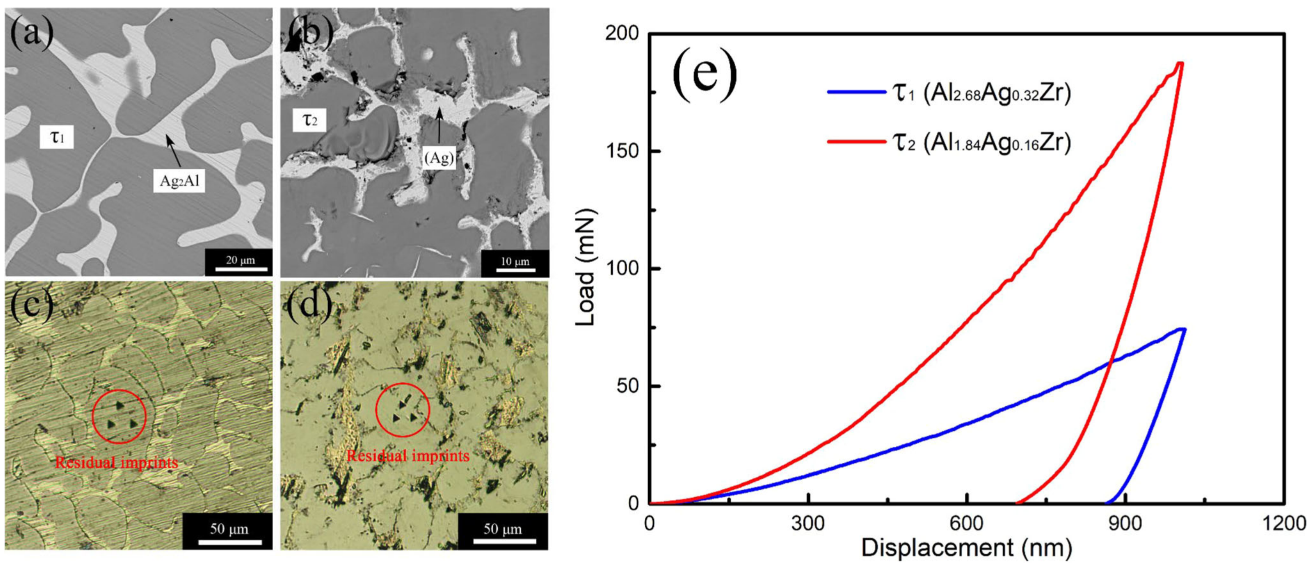

Figure 15 BEI (**a**, **b**) and Metallographic (**c**, **d**) images for alloy samples. (**e**) Load–displacement curves for indentation into grains of the intermetallic phases τ_1 and τ_2.

Table 7 Hardness of τ_1 and τ_2 phases et al.-rich ends

Phase	Hardness (GPa)			
	1	2	3	Average value
τ_1	3.90	3.81	3.76	3.82
τ_2	10.16	10.32	10.12	10.20

Acknowledgements

This work was supported by National Natural Science Foundation of China (Grant Nos. 51871248 and 52071339), and Natural Science Foundation of Hunan Province, China (Grant No. 2020JJ4739). We are grateful for resources from the High Performance Computing Center of Central South University.

Author contributions

ZD contributed to experimental determination, data analysis, first-principles calculations, thermodynamic optimization, writing—original draft. YD contributed to experimental determination. PM contributed to writing—review and editing. KW contributed to sample preparation. LZ contributed to resources and funding acquisition. LL contributed to project administration and funding acquisition.

Data availability

Data available on request from the authors.

Declarations

Conflict of interest The authors declare that they have no known competing financial interests or personal relationships that could have appeared to influence the work reported in this paper.

Supplementary Information: The online version contains supplementary material available at https://doi.org/10.1007/s10853-023-08665-3.

References

[1] Hu B, Quan BB, Li DJ, Wang XY, Li ZX, Zeng XQ (2021) Solid solution strengthening mechanism in high pressure die casting Al–Ce–Mg alloys. Mater Sci Eng A 812:141109. https://doi.org/10.1016/j.msea.2021.141109

[2] De LA, DaN S, Dunand DC (2020) Mn and Mo additions to a dilute Al–Zr–Sc–Er–Si-based alloy to improve creep resistance through solid-solution- and precipitation-strengthening. Acta Mater 194:60–67. https://doi.org/10.1016/j.actamat.2020.04.022

[3] Masuda T, Sauvage X, Hirosawa S, Horita Z (2020) Achieving highly strengthened Al–Cu–Mg alloy by grain refinement and grain boundary segregation. Mater Sci Eng A 793:139668. https://doi.org/10.1016/j.msea.2020.139668

[4] Schliephake D, Lopes C, Eggeler YM, Chen H, Freudenberger J, Bayoumy D, Huang AJ, Kauffmann A (2022) Improved work hardening capability and ductility of an additively manufactured and deformed Al–Mn–Mg–Sc–Zr alloy. J Alloys Compd 924:166499. https://doi.org/10.1016/j.jallcom.2022.166499

[5] Shaha SK, Czerwinski F, Kasprzak W, Chen DL (2014) Work hardening and texture during compression deformation of the Al–Si–Cu–Mg alloy modified with V, Zr and Ti. J Alloys Compd 593:290–299. https://doi.org/10.1016/j.jallcom.2013.12.081

[6] Yang Z, Zhang ML, Fan LY, Bai JY, Chen XL, Zhang J, Li Z, Guan RG (2023) Towards high mechanical performance Al–Cu–Mg–Fe–Ni alloy: influence of composition, solution treatment and aged process on microstructural evolution and mechanical properties. J Mater Res Technol 23:2054–2064. https://doi.org/10.1016/j.jmrt.2023.01.166

[7] Dar SM, Liao HC (2019) Creep behavior of heat resistant Al–Cu–Mn alloys strengthened by (θ′) and coarse (Al_{20}-Cu_2Mn_3) second phase particles. Mater Sci Eng A 763:138062. https://doi.org/10.1016/j.msea.2019.138062

[8] Ekaputra CN, Rakhmonov JU, Weiss D, Mogonye JE, Dunand DC (2022) Microstructure and mechanical properties of cast Al–Ce–Sc–Zr–(Er) alloys strengthened by Al11Ce3 micro-platelets and L12 Al3(Sc, Zr, Er) nano-precipitates. Acta Mater 240:118354. https://doi.org/10.1016/j.actamat.2022.118354

[9] Reich L, Murayama M, Hono K (1998) Evolution of Ω phase in an Al–Cu–Mg–Ag alloy—a three-dimensional atom probe study. Acta Mater 46:6053–6062

[10] Ou YZ, Jiang Y, Wang YR, Liu ZQ, Lervik A, Holmestad R (2021) Vacancy and solute co-segregated η_1 interface in over-aged Al–Zn–Mg alloys. Acta Mater 218:117082. https://doi.org/10.1016/j.actamat.2021.117082

[11] Voorhees PW (2006) Scandium overtakes zirconium. Nat Mater 5:435–436

[12] Elgallad EM, Shen P, Zhang Z, Chen XG (2014) Effects of heat treatment on the microstructure and mechanical properties of AA2618 DC cast alloy. Mater Des 61:133–140. https://doi.org/10.1016/j.matdes.2014.04.045

[13] Shen ZJ, Liu CH, Ding QQ, Wang SB, Wei X, Chen L, Li JX, Zhang Z (2014) The structure determination of Al_{20}-Cu_2Mn_3 by near atomic resolution chemical mapping. J Alloys Compd 601:25–30. https://doi.org/10.1016/j.jallcom.2014.02.125

[14] Deng ZX, Hu Q, Tian YY, Xue RH, Zhang LG, Liu LB (2023) Experimental investigation and thermodynamic assessment of the Al–Ag–Sc system. J Alloys Compd 934:167980. https://doi.org/10.1016/j.jallcom.2022.167980

[15] De LA, Dunand DC, Seidman DN (2016) Mechanical properties and optimization of the aging of a dilute Al–Sc–Er–Zr–Si alloy with a high Zr/Sc ratio. Acta Mater 119:35–42. https://doi.org/10.1016/j.actamat.2016.08.018

[16] Wang LY, Ye B, Bai Y, Zhao BB, Ding WJ (2021) Effect of Zr and Sc micro-additions on the microstructure and mechanical properties of as-cast Al–5Ce alloy. Mater Sci Eng A 822:141654. https://doi.org/10.1016/j.msea.2021.141654

[17] Kotur B, Verbovytsky Y (2003) Phase equilibria in the {Zr, Hf}–Ag–Al systems at 500 °C and crystal structure of the ternary compounds. Prace Nauk WSP Chem 8:7

[18] Hsiao HM, Lan YC, Hermana GN, Chen H, Yen YW (2018) Investigation of the phase equilibria at 773 K and metallic glass regions in the Ag–Al–Zr ternary system. MRS Commun 8:113–121. https://doi.org/10.1557/mrc.2017.134

[19] Witusiewicz VT, Hecht U, Fries SG, Rex S (2004) The Ag–Al–Cu system: Part I: reassessment of the constituent binaries on the basis of new experimental data. J Alloys Compd 385:133–143. https://doi.org/10.1016/j.jallcom.2004.04.126

[20] Fischer E, Colinet C (2015) An updated thermodynamic modeling of the Al–Zr system. J Phase Equilib Diffus 36:404–413. https://doi.org/10.1007/s11669-015-0398-y

[21] McPherson DJ, Hansen M (1954) The system zirconium aluminum. Trans Am Soc Met 46:354–374

[22] Peruzzi A (1992) Reinvestigation of the Zr-rich end of the Zr-Al equilibrium phase diagram. J Nucl Mater 186:89–99

[23] Saunders N, Rivlin VG (1986) Thermodynamic characterization of Al–Cr, Al–Zr, and Al–Cr–Zr alloy systems. Mater Sci Technol 2:520–527

[24] Saunders N (1989) Calculated stable and metastable phase equilibria in Al–Li–Zr Alloys/Berechnung der stabilen und metastabilen phasengleichgewichte in Al–Li–Zr-legierungen. Int J Mater Res 80:894–903

[25] Wang T, Jin ZP, Zhao JC (2001) Thermodynamic assessment of the Al–Zr binary system. J Phase Equilib 22:544–551

[26] Hsiao HM, Liang SM, Schmid-Fetzer R, Yen YW (2016) ‘Thermodynamic assessment of the Ag–Zr and Cu–Zr binary systems. Calphad 55:77–87. https://doi.org/10.1016/j.calphad.2016.08.001

[27] Raub EV, Engel M (1948) Alloys of zirconium with copper, silver, and gold. Z Metallkd 39:172–177

[28] Betterton JJ, Easton DS (1958) The silver-zirconium system. Trans Met Soc AIME, p. 212

[29] Zhang KH, Zhao HZ, Zhou YH (1988) An investigation of the Ag–Zr phase diagram. J Less-Common Met 138:173–177

[30] Karakaya I, Thompson WT (1992) The Ag–Zr (silver-zirconium) system. J Phase Equilib 13:143–146

[31] Kang DH, Jung IH (2010) Critical thermodynamic evaluation and optimization of the Ag–Zr, Cu–Zr and Ag–Cu–Zr systems and its applications to amorphous Cu–Zr–Ag alloys. Intermetallics 18:815–833

[32] Bale CW, Chartrand P, Degterov SA, Eriksson G, Hack K, Mahfoud RB, Melançon J, Pelton AD, Petersen S (2002) FactSage thermochemical software and databases. Calphad 26:189–228

[33] Chen SL, Daniel S, Zhang F, Chang Y, Yan XY, Xie FY, Schmid-Fetzer R, Oates W (2002) The PANDAT software package and its applications. Calphad 26:175–188

[34] Sundman B, Jansson B, Andersson JO (1985) The thermo-calc databank system. Calphad 9:153–190

[35] Rieger W, Nowotny H, Benesovsky F (1964) Kristallchemische untersuchungen in systemen mit T-elementen,(Cu, Ag) und (Al, Ga). Monatshefte für Chemie und verwandte Teile anderer Wissenschaften 95:1573–1576

[36] Villars P, Calvert LD, Pearson WB (1985) Pearson's handbook of crystallographic data for intermetallic phases. Acta Cryst 40:C444

[37] Massalski TB (1990) Binary alloy phase diagrams, 2nd edn. Materials Park, Ohio, p 2705–2708

[38] King HW (1981) Crystal structures of the elements at 25 °C. Bull Alloy Phase Diagr 2:401–402

[39] Massalski TB, Murray J, Bennett L, Baker H (1986) Binary alloy phase diagrams. vol. i and ii. American Society for Metals, p. 2224

[40] Murray J, Peruzzi A, Abriata J (1992) The Al–Zr (aluminum–zirconium) system. J Phase Equilib 13:277–291

[41] Schmid-Fetzer R (2003) Al–Ti (Aluminium–Titanium)', MSIT binary evaluation program. MSIT Workplace

[42] Endo N, Kameoka S, Tsai AP, Zou LL, Hirata T, Nishimura C (2010) Hydrogen absorption in the intermetallic compounds Zr_2TM (TM = Cu, Ag and Au) with $MoSi_2$-type structure (C11b). J Alloys Compd 490:L24–L27

[43] Dinsdale AT (1991) SGTE data for pure elements. Calphad 15:317–425

[44] Redlich O, Kister A (1948) Algebraic representation of thermodynamic properties and the classification of solutions. Ind Eng Chem 40:345–348

[45] Kresse G, Furthmüller J (1996) Efficient iterative schemes for ab initio total-energy calculations using a plane-wave basis set. Phys Rev B 54:11169

[46] Du Y, Schmid-Fetzer R, Ohtani H (1997) Thermodynamic assessment of the VN system. Z Metallkd 88:545–556